Source-Rupture Process of the 2007 Noto Hanto, Japan, Earthquake Estimated by the Joint Inversion of Strong Motion and GPS Data

AUTHOR(S):

Asano, Kimiyuki; Iwata, Tomotaka

CITATION:

Asano, Kimiyuki ...[et al]. Source-Rupture Process of the 2007 Noto Hanto, Japan, Earthquake Estimated by the Joint Inversion of Strong Motion and GPS Data. Bulletin of the Seismological Society of America 2011, 101(5): 2467-2480

ISSUE DATE:

2011-09-26

URL:

http://hdl.handle.net/2433/209745

Bulletin of the Seismological Society of America

SSA
THE SEISMOLOGICAL SOCIETY OF AMERICA
400 Evelyn Ave., Suite 201
Albany, CA 94706-1375
(510) 525-5474; FAX (510) 525-7204
www.seismosoc.org

Bulletin of the Seismological Society of America, Vol. 101, No. 5, pp. 2467–2480, October 2011, doi: 10.1785/0120100254

Source-Rupture Process of the 2007 Noto Hanto, Japan, Earthquake Estimated by the Joint Inversion of Strong Motion and GPS Data

by Kimiyuki Asano and Tomotaka Iwata

Abstract The source-rupture process during the 2007 Noto Hanto earthquake, which was a reverse-faulting event located near the western coast of the Noto peninsula in central Japan, was estimated by the kinematic linear waveform inversion method. The waveform inversion was conducted by jointly using velocity waveforms recorded at 12 near-source strong-motion stations and static horizontal displacements recorded at 19 Global Positioning System (GPS) stations. In order to implement reliable Green's functions into the inversion, a one-dimensional underground velocity structure for each individual strong-motion station was modeled through waveform modeling of an aftershock. The waveform inversion result showed the following image of the source-rupture process. The larger slip concentrated in the vicinity of the hypocenter, and it extended to the shallow portion of the source fault with a maximum slip of 5.1 m. The whole source process was characterized by the total seismic moment of 1.57×10^{19} N·m (M_w 6.7) with the rupture duration of approximately 9 s. The obtained source model explained observed strong ground motions and GPS-measured static horizontal displacements well. The slip distribution correlated well with the spatiotemporal aftershock distribution, and the northeast end of the rupture was blocked by the resistive structure in the crust. From these facts, the 2007 Noto Hanto earthquake could be concluded as reactivation of preexisting seafloor active faults, F14 and F15, which were reported by the previous geophysical and geological surveys off the shore of the Noto peninsula.

Introduction

The 2007 Noto Hanto earthquake (M_{JMA} 6.9) occurred near the western coast of the Noto peninsula (Noto Hanto in Japanese), central Japan (Fig. 1) at 09:41 on 25 March 2007, Japan Standard Time (JST; 00:41 on 25 March, coordinated universal time [UTC]). The focal mechanism obtained in the moment tensor solution of F-net (Fukuyama *et al.*, 1998), which is operated by the National Research Institute for Earth Science and Disaster Prevention, Japan (NIED), revealed that the strike, dip, and rake angles were 58°, 66°, and 132°, respectively. This event was a reverse-fault-type crustal earthquake including right-lateral strike-slip motions with northwest–southeast compression. The intensive temporary aftershock observation also revealed a high dip-angle fault structure dipping in the southeast direction (Kato *et al.*, 2008; Sakai *et al.*, 2008).

The strong ground motions during this event caused significant damage over a wide area in the Noto peninsula, including Wajima city and Anamizu town, for wooden houses in particular, which are typical residences in Japan (e.g., Nishida *et al.*, 2007; Yamada *et al.*, 2008). These strong ground motions were densely observed by the nationwide digital strong-motion seismograph networks, K-NET (Kinoshita, 1998) and KiK-net (Aoi *et al.*, 2000), both installed by NIED. A peak ground velocity of 103 cm/s was observed during the mainshock at a K-NET strong-motion station, ISK005, in Anamizu town. The crustal movements associated with the faulting were also observed by the Global Positioning System (GPS) of the GPS Earth Observation Network System (GEONET) deployed by the Geospatial Information Authority of Japan (GSI).

The generation of such a shallow crustal earthquake is widely thought to be related to the Quaternary active fault and active folding system. The existence of seafloor fault traces off the western coast of the Noto peninsula has been reported in the previous geophysical and geological surveys (Katagawa *et al.*, 2005; Okamura, 2007). Katagawa *et al.* (2005) have discovered northeast-southwest–trending Quaternary reverse faults beneath the sea in the source region of the 2007 Noto Hanto earthquake by sonic prospecting and piston coring. Most aftershocks of the 2007 Noto Hanto earthquake appear to have occurred along these fault traces.

The main purpose of this paper is to investigate the source-rupture process of the 2007 Noto Hanto earthquake by jointly analyzing near-source strong ground motion

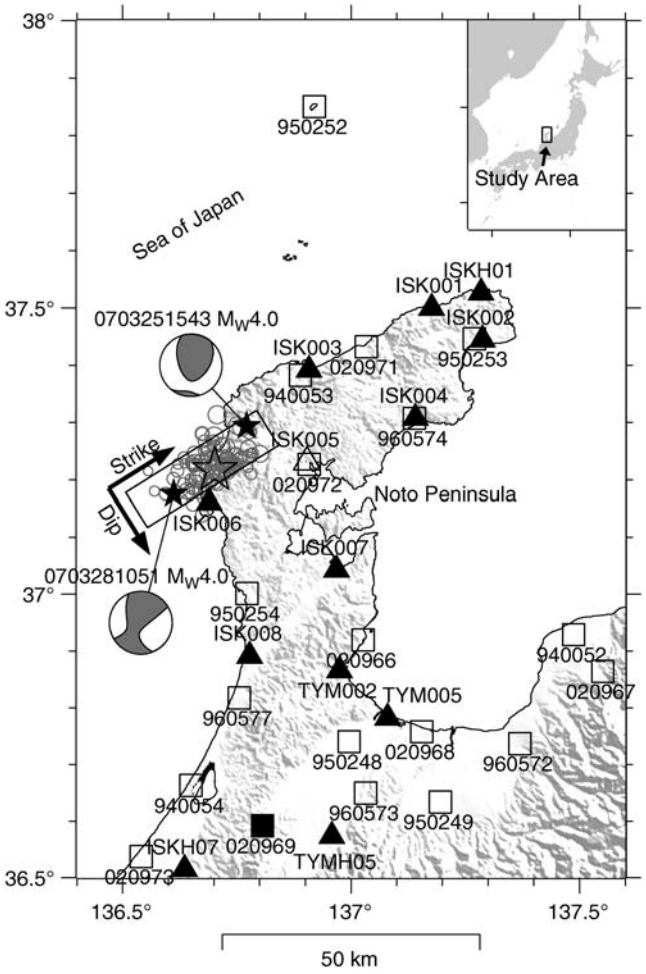

Figure 1. Distribution of 12 strong-motion stations (solid triangles) and 19 GPS stations (open squares) used in this study. ISK005 is also represented by the open triangle, and the reference site of GPS data is indicated by the solid square. The open star indicates the epicenter of the 2007 Noto Hanto earthquake. The rectangle corresponds to the surface projection of the fault-plane model assumed for the source inversion. The aftershocks used in velocity-structure modeling are also shown by the solid star with its moment tensor determined by F-net, NIED in the lower hemisphere projection. The small open circles correspond to the epicenters of aftershocks greater than M_{JMA} 2.0 within 1 hr after the mainshock.

and GPS data. Firstly, one-dimensional velocity-structure models for each of the strong-motion stations are estimated by waveform modeling of a small event in order to prepare reliable Green's functions. Then, the source-rupture process during the mainshock is obtained by the kinematic linear waveform inversion using both strong-motion velocity waveforms and GPS-measured static horizontal-displacement data. Finally, the relationship between the slip distribution obtained by the waveform inversion and the preexisting active-fault structure is discussed.

Data Processing

Strong ground motion time series observed by strong-motion seismographs and static displacements observed by GPS are jointly used to deduce the kinematic source-rupture process of this earthquake. Near-source strong ground motion data have great ability to retrieve detailed temporal progression of the rupture, and GPS-measured static data have a potential to constrain precisely the amount of final slip on the fault. Moreover, the combined use of strong-motion and GPS data can generally increase the frequency band covered by the inversion analysis and gives a more stable solution (e.g., Wald and Graves, 2001; Asano *et al.*, 2005). Particularly, the seismic moment may be constrained well by use of static GPS data.

For strong-motion data, three components of time-series data from nine stations of K-NET and three stations of KiK-net within 80 km from the epicenter are used in the source-inversion analysis (Table 1). The distribution of the stations is mapped by solid triangles in Figure 1. The K-NET stations have surface sensors only. The K-NET ISK005 is not used, because clear nonlinear site response during the mainshock has been reported for this station (e.g., Iwata *et al.*, 2008). For KiK-net stations, data from downhole sensor is used to reduce the effect of subsurface soft layers. The depth of the downhole sensor ranges from 144 to 802 m by station (Table 1). The original acceleration time histories of K-NET stations were sampled at 100 Hz, and those of KiK-net stations were sampled at 200 Hz. The ground acceleration is integrated into ground velocity in the time domain and band-pass filtered with a sixth-order Chebyshev Type I recursive filter with a zero-phase shift between 0.05 and 1.0 Hz. Then, the velocity-waveform data are resampled at 10 Hz. The dataset in the source inversion comprises 20 s of the time series from 1 s before the direct *S*-wave arrival, which is carefully picked up by visual inspection. The common duration of the time series is given to all the strong-motion stations to make the number of data samples equal among the stations. The exclusion of the *P* phase will not significantly affect the source-inversion result (Asano and Iwata, 2009).

For GPS-measured static displacement data, daily coordinate data from 19 GPS observation stations belonging to GEONET, which is routinely released from GSI, are used

Table 1
List of Strong Motion Stations Used in This Study

Station	Latitude (°N)	Longitude (°E)	Depth (m)	Network	Location
ISK001	37.4999	137.1764	0	K-NET	Ohya
ISK002	37.4443	137.2877	0	K-NET	Shohin
ISK003	37.3919	136.9083	0	K-NET	Wajima
ISK004	37.3080	137.1470	0	K-NET	Noto
ISK006	37.1602	136.6897	0	K-NET	Togi
ISK007	37.0427	136.9681	0	K-NET	Nanao
ISK008	36.8918	136.7783	0	K-NET	Hakui
TYM002	36.8660	136.9747	0	K-NET	Himi
TYM005	36.7824	137.0803	0	K-NET	Shinminato
ISKH01	37.5266	137.2844	200	KiK-net	Suzu
ISKH07	36.5150	136.6357	802	KiK-net	Kanazawa
TYMH05	36.5736	136.9584	144	KiK-net	Inami

(open squares in Fig. 1). Following Ishimoto and Yutsudo (2007), the coseismic static displacement is estimated by subtracting the average daily coordinates over seven days preceding 25 March 2007 from the average daily coordinates over six days after 25 March 2007 relative to the station 020969 (Fukumitsu station), whose location is indicated by the solid square in Figure 1. Two horizontal displacement components (east–west and north–south) are used in the source inversion.

Modeling of Velocity Structure for Each Strong Motion Station

Observed ground motions are theoretically represented as the convolution of source, path, and site effects. Therefore, construction of a reliable velocity-structure model is essentially important in kinematic source inversions. Because near-source strong ground motions are greatly affected by the subsurface low-velocity sedimentary layers beneath the station, it is desired to consider the difference of subsurface structures among strong-motion stations. Asano and Iwata (2009) proposed a procedure to improve Green's function for the source inversion by modeling waveforms of small aftershock events, and they demonstrated the importance of velocity-structure modeling to obtaining a stable solution in the kinematic source inversion. They applied their method to the 2004 Chuetsu, Mid-Niigata prefecture, Japan, earthquake (M_w 6.6), which occurred in the region of active folding mountain system with complicated deep sedimentary structure, and succeeded in obtaining a reliable image of the source-rupture process.

In this study, one-dimensional underground velocity-structure models for each strong-motion station are prepared following Asano and Iwata (2009). According to their study, an individual one-dimensional velocity-structure model is estimated for each strong-motion station as an approximation of a real three-dimensional earth structure. Firstly, a reference layered underground structure model is assumed over the whole area based on previous exploration studies. The reference velocity-structure model comprises some sedimentary layers above the bedrock. The material parameters of each layer (elastic wave velocity, density, Q value) are assumed and fixed in advance. Then, appropriate thickness of each sedimentary layer is searched separately for each station using the genetic algorithm (GA; Holland, 1975). The velocity, density, and Q structure for the crust and upper mantle is common to all stations. The goodness of the waveform fit is evaluated by the following misfit function first proposed by Sen and Stoffa (1991):

$$f(\tau) = 1.0 - 2\frac{\int u(t)_{\mathrm{obs}} u(t+\tau)_{\mathrm{syn}} dt}{\int [u(t)^2_{\mathrm{obs}} + u(t+\tau)^2_{\mathrm{syn}}] dt}. \qquad (1)$$

Here, $u(t)_{\mathrm{obs}}$ and $u(t)_{\mathrm{syn}}$ are the observed and synthetic waveforms, respectively. τ is the time shift to compensate for the error in the absolute travel time between observation and synthetics due to the factors that are not explained by this simple one-dimensional model. This discrepancy is because any one-dimensional velocity model is just an approximation of the true, three-dimensional heterogeneous velocity structure in the Earth. Each thickness is coded as a binary number with five bits so that each parameter can take 32 possible values. The step size of the parameters ranges from 1 to 50 m depending on the layer. The initial population that consists of 40 models for GA is randomly generated, and the evolution process, which includes the tournament selection, uniform crossover, jump and creep mutation, and elitism, is applied to the population to reproduce the next generation with the same population size using the algorithm developed by Carroll (1996). Each evolution process is terminated at the fiftieth generation. After five runs starting with different initial models, the best model is accepted as the final solution.

The reference underground velocity-structure model assumed is listed in Table 2. The model parameters are set referring to previous exploration studies by Kanno *et al.* (2003) for sedimentary layers and Aoki *et al.* (1972) for the crust and upper mantle. In addition, some superficial low-velocity layers at each station are also included from the borehole *PS* logging information released by K-NET and KiK-net. The layer thicknesses of this superficial portion are fixed at values given by the logging data, and they are not changed in this study. That is, the shear-wave velocity at the ground surface is smaller than 700 m/s according to the logging data. The *PS* logging information is available down to 20 m for K-NET stations, and whole *PS* logging information above the downhole sensor is open to the public for KiK-net stations. If the V_S at the bottommost layer of the logging profile was faster than 700 m/s, we removed the first layer with the V_S of 700 m/s from the model in Table 2 and

Table 2
Reference Underground Structure Model

Layer	Depth (m)	V_P (m/s)	V_S (m/s)	ρ (kg/m^3)	Q_P	Q_S
1	0	2000	700	1980	100	50
2	variable	3100	1200	2200	200	100
3	variable	4500	2100	2480	400	200
4	variable	5500	3180	2600	600	300
upper crust	5000	6000	3460	2700	700	350
lower crust	18000	6600	3800	2900	800	400
upper mantle	30000	7800	4500	3100	1000	500

inverted for the remaining layers. The theoretical Green's functions are calculated by the discrete wavenumber method (Bouchon, 1981) with the reflection and transmission matrix (Kennett and Kerry, 1979). This calculation method gives a full Green's function.

The dataset from an aftershock (M_w 4.0) that occurred at 15:43 on 25 March 2007 (JST) is used for modeling of the velocity structure. The target of the misfit function is velocity waveforms in 0.05–1 Hz. The epicenter is fixed at 37.2940° N, 136.7718° E, which was located by the Japan Meteorological Agency (JMA). The depth of the point source is assumed to be 5 km, which is the centroid depth determined by F-net. The moment tensor released by F-net is adopted as a point source (see Fig. 1). The source duration time is set to be 0.2 s, which is determined to fit the observed pulse width of the direct *S*-wave portion.

The velocity-structure models for 12 strong-motion stations shown in Figure 1 are estimated in this study. In Figure 2, the synthetic velocity waveforms at ISK001 and ISK008 calculated from the best velocity-structure model (improved model) are compared with the observed records. The synthetics without a detailed structure of the sedimentary layers (rock model) are also plotted together. The ISK008 is located in the Ochigata plain, which has relatively deep sedimentary parts as shown in Figure 3. It can be seen that the characteristics of observed waveforms are explained well by the improved model compared to the rock model in terms of amplitude and duration. Figure 3 shows the obtained velocity-structure models for all of the strong-motion stations. The models whose goodness of waveform fit is greater than 90% of that of the best model are also represented by thin gray lines in this figure. The estimated bedrock depth ranges from 334 to 1880 m. The theoretical velocity waveforms in 0.05–1 Hz calculated from the obtained velocity-structure models are plotted with the observed velocity waveforms in Figure 4. In order to check the feasibility of this velocity-structure modeling, a comparison of theoretical and observed velocity waveforms in the same frequency range for another aftershock with M_w 4.0, which has not been directly used in the velocity-structure modeling in this paper, is presented in Figure 5. This aftershock occurred at 10:51 on 28 March 2007 (JST) at the depth of 5 km southwest of the epicenter (Fig. 1). As detailed information of bedrock depth distribution is not available in this area, accuracy of the obtained one-dimensional velocity-structure models could not be judged. However, the synthetic waveforms reproduced observed velocity-structure models fairly well in the frequency range considered particularly in terms of the amplitude of the direct *S*-wave portion (Figs. 4 and 5), and it can be concluded that our simple one-dimensional velocity-structure models obtained here may be adequately used as an approximation of true three-dimensional subsurface structure for the calculation of Green's functions in the source inversion.

Source-Inversion Method and Fault-Model Settings

The source-rupture process during the mainshock is estimated by the kinematic linear waveform inversion with multiple time windows (Hartzell and Heaton, 1983). A single planar fault model is assumed in accordance with the

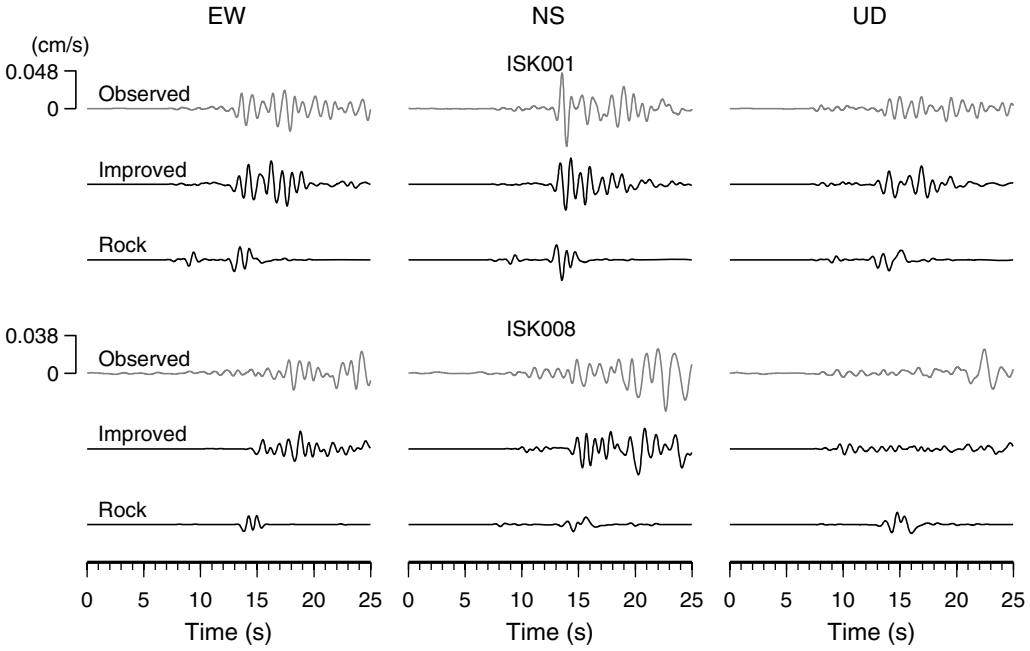

Figure 2. Comparison of observed and theoretical velocity waveforms (0.05–1 Hz) of the M_w 4.0 aftershock used in the modeling of the velocity structure at ISK001 and ISK008. Improved means the theoretical waveforms calculated from the best velocity-structure model estimated in this study. Rock means the theoretical waveforms calculated from a velocity-structure model without sedimentary layers.

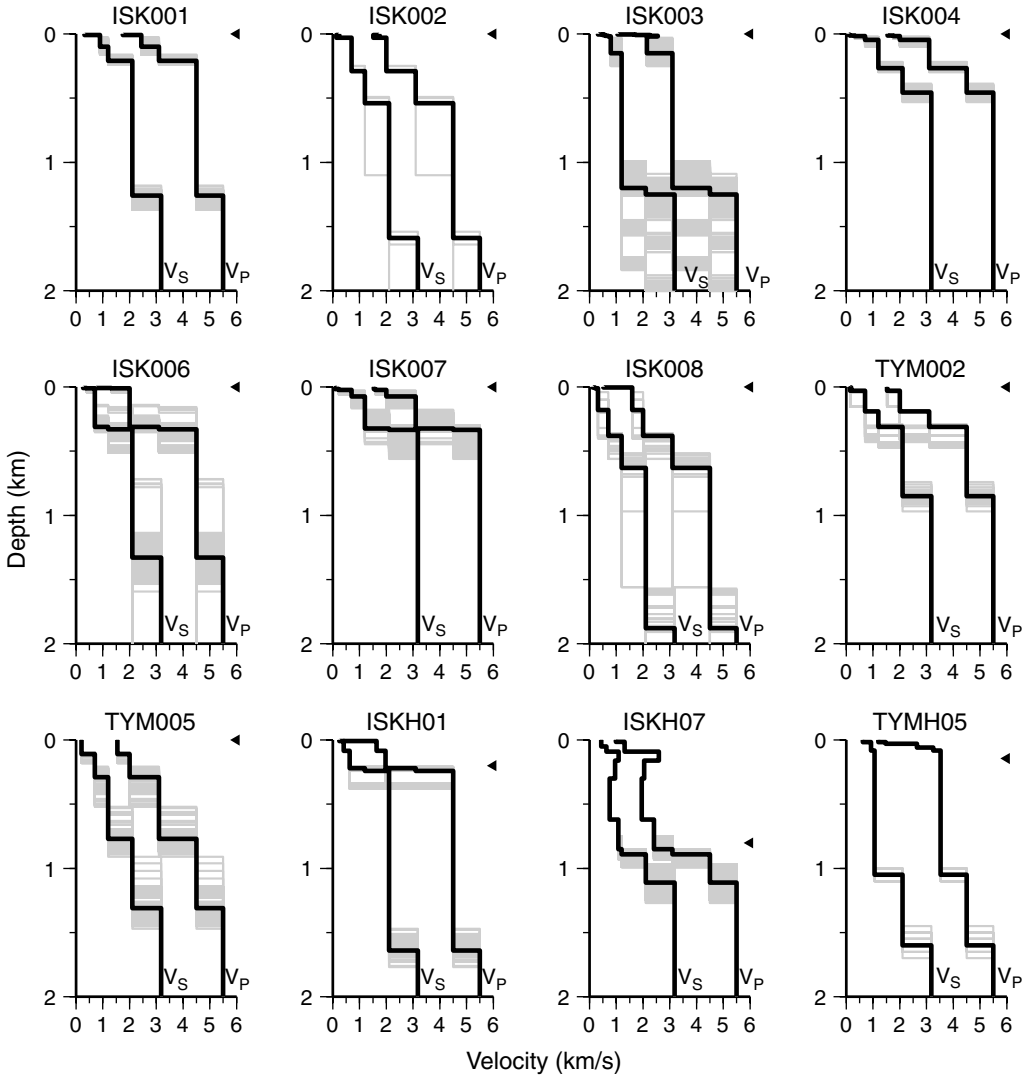

Figure 3. Best velocity-structure model above the bedrock estimated by modeling aftershock waveforms using GA (thick bold line) and models whose goodness values are more than 90% of that of the best model (thin gray lines) for each strong-motion station. The left-triangle indicates the depth where the sensor is installed.

aftershock distributions. The length along strike and width along dip of the fault plane are 30 and 16 km, respectively. The rupture starting point is fixed at 37.21698° N, 136.70192° E at a depth of 9.62 km, which is the hypocenter relocated by Sakai *et al.* (2008). This point corresponds to the location of the precursor, which occurred 0.6 s before the mainshock in the original relocated parameters by Sakai *et al.* (2008). In the waveform inversion, the precursor portion is analyzed together with the whole ground motion from the mainshock. Sakai *et al.* (2008) estimated the magnitude of the precursor to be 4.4, much smaller than the mainshock. The precursor and the mainshock hypocenter collocated in the same subfault, so the moment-rate function estimates at the hypocenter includes the contribution from the precursor as a sequence of moment release. The strike and dip angles of the fault plane are respectively assumed to be 58° and 60° following the aftershock distribution. The fault plane is divided into 120 subfaults of 2 km × 2 km (15 along the strike and 8 along the dip).

The temporal moment-release history at each subfault is expressed by a series of six smoothed ramp functions assigned at the center of the subfault, in which each smoothed ramp function has the duration of 1.0 s and is separated by 0.5 s. The unknown model parameters are the amplitude of the smoothed-ramp functions corresponding to each time window at each subfault. The rupture front-propagation velocity triggering the rupture of the first time window at each subfault is selected so as to minimize the residual of data fitting. Six values of the rupture front propagation velocity, 2.08, 2.25, 2.42, 2.60, 2.77, and 2.94 km/s, are tested here. They correspond to 60%, 65%, 70%, 75%, 80%, and 85% of the shear-wave velocity at the hypocenter, respectively. Rake angle variations are limited within 135° ± 45° using the nonnegative constraint (Lawson and Hanson, 1974). The detailed

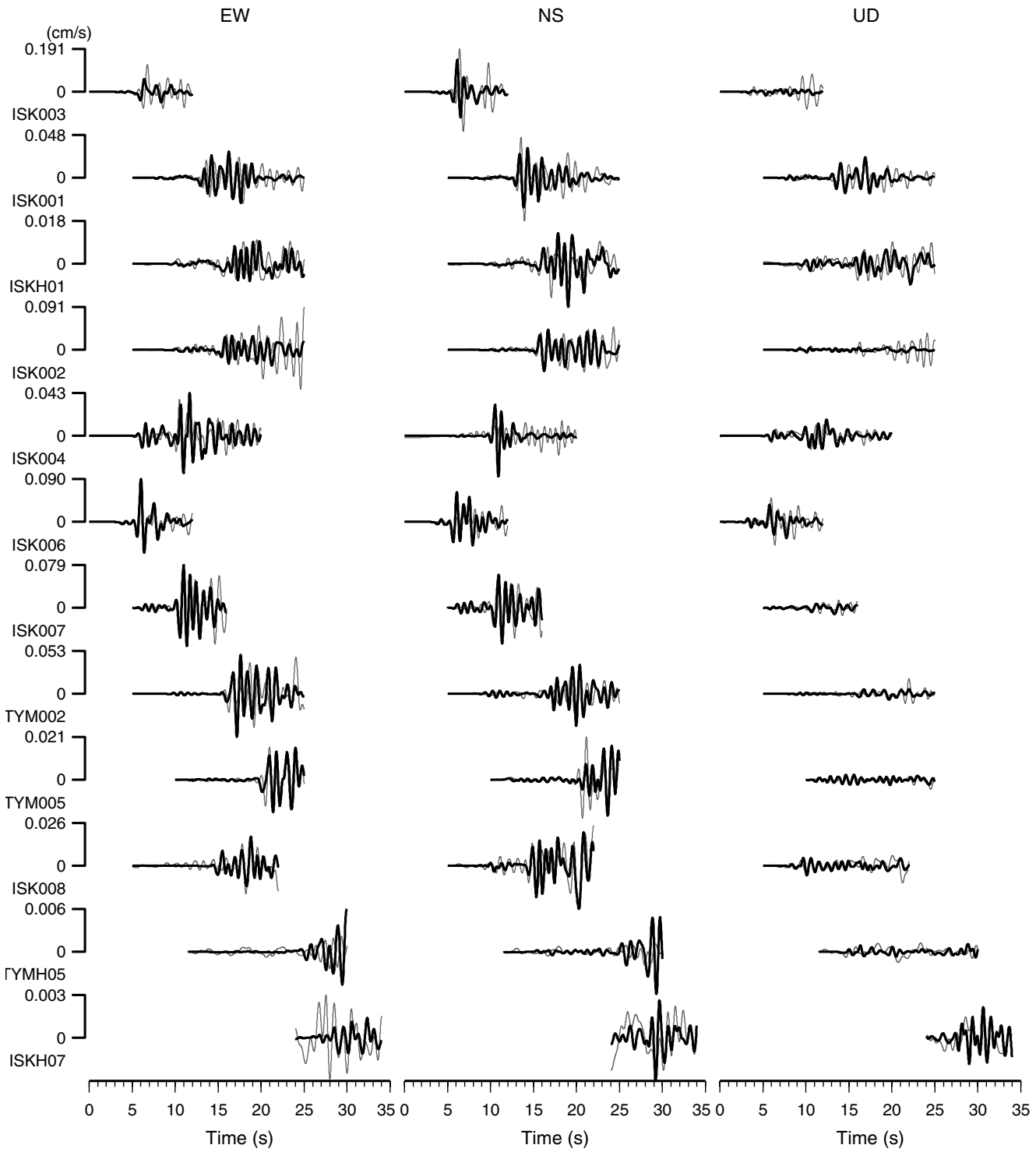

Figure 4. Comparison of velocity waveforms (0.05–1 Hz) of the M_w 4.0 aftershock at 15:43 on 25 March 2007 (JST) used in velocity-structure modeling between observed waveforms (gray line) and synthesized waveforms (solid black line) at each strong-motion station. The amplitude is normalized by the maximum amplitude for each station. EW, east–west; NS, north–south; UD, up–down.

description of the joint inversion method employed here can be found in Asano *et al.* (2005). Following is a brief introduction to the inversion method in this study.

The observational equation for strong-motion data is

$$\mathbf{Gm} \cong \mathbf{d}_{\mathrm{SM}}. \quad (2)$$

Here, $\mathbf{m}$ is an N-dimensional model parameter vector composed of the amount of moment release at each time window at each subfault. $\mathbf{G}$ is an $M_G \times N$ coefficient matrix whose elements are discretized-theoretical Green's functions from each subfault to each strong-motion station. $\mathbf{d}_{\mathrm{SM}}$ is an

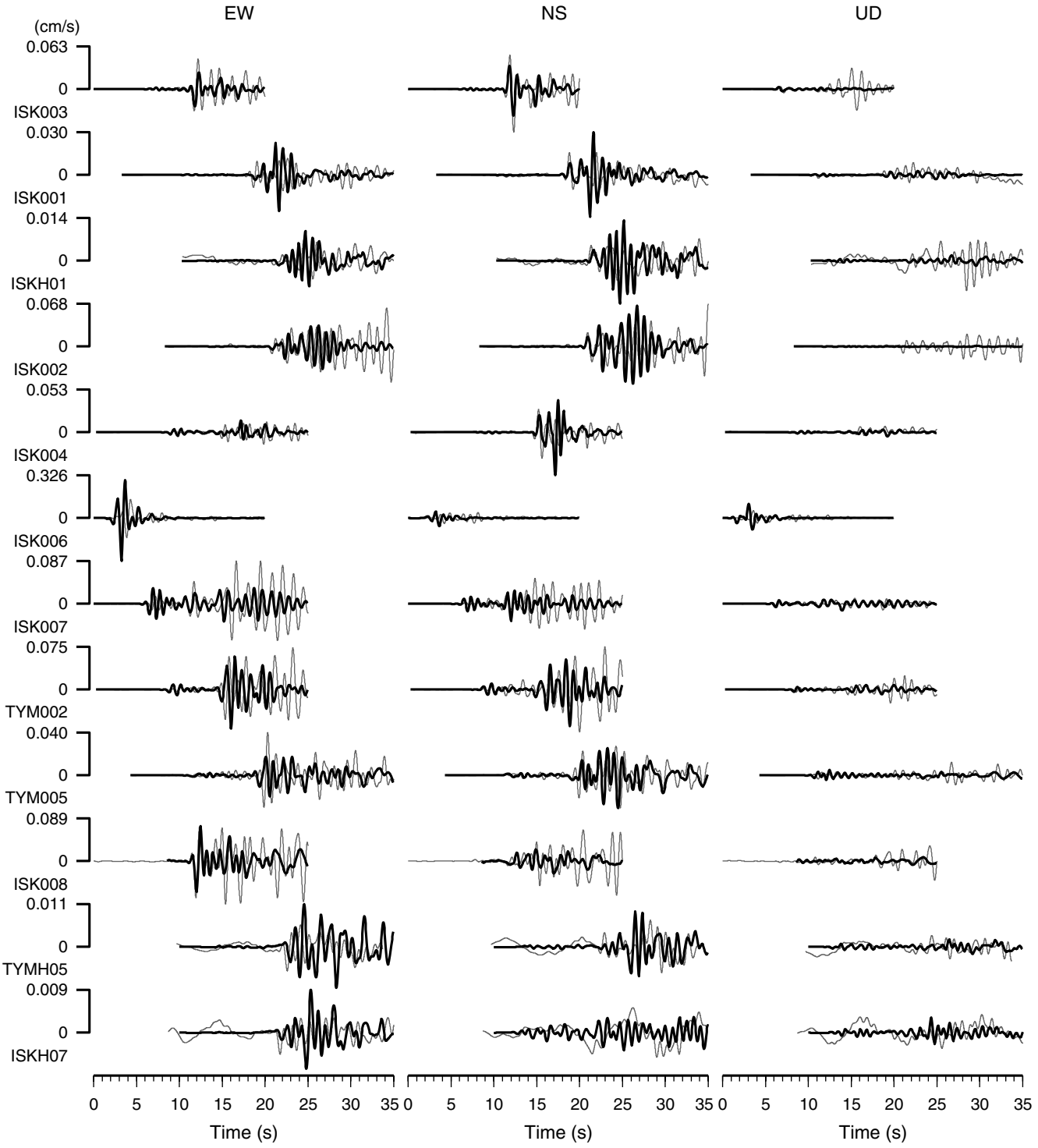

Figure 5. Comparison of velocity waveforms (0.05–1 Hz) of the M_w 4.0 aftershock at 10:51 on 28 March 2007 (JST) not used in velocity-structure modeling between observed (gray line) and synthesized waveforms (solid black line) at each strong-motion station. The amplitude is normalized by the maximum amplitude for each station. EW, east–west; NS, north–south; UD, up–down.

M_G-dimensional data vector composed of a discretized-velocity time series at strong-motion stations. The theoretical Green's functions for strong-motion stations are calculated using the set of underground structure models estimated in the previous section. The amplitudes of observed and theoretical velocity waveforms at individual stations are normalized by the maximum amplitude of its observed velocity waveform so that the stations with larger amplitude do not dominate the solution. The observational equation for GPS data is

$$\mathbf{Hm} \cong \mathbf{d}_{\mathrm{GPS}}. \tag{3}$$

Here, $\mathbf{H}$ is an $M_H \times N$ coefficient matrix whose elements are horizontal components of theoretical Green's functions from each subfault to each GPS station. $\mathbf{d}_{\mathrm{GPS}}$ is an M_H-dimensional data vector composed of horizontal static displacements at GPS stations. Green's functions for GPS data are calculated by assuming a uniform-layered underground-structure model. The normalization or equal weighting is not applied to GPS data to avoid the instability (Wald and Graves, 2001).

In order to obtain a stable solution, the spatiotemporal smoothing constraint to reduce instability or excess of complexity is also included in the analysis following Sekiguchi *et al.* (2000). Their smoothing constraint equation assumes the model parameters close both in space and in time to be similar. The smoothing constraint equations in matrix form are expressed by

$$\mathbf{Sm} \cong 0. \tag{4}$$

$\mathbf{S}$ is an $M_S \times N$ matrix whose elements are coefficients of smoothing constraint equations.

The above observational and smoothing constraint equations can be combined as

$$\begin{pmatrix} \mathbf{G} \\ \alpha\mathbf{H} \\ \beta\mathbf{S} \end{pmatrix} \mathbf{m} \cong \begin{pmatrix} \mathbf{d}_{\mathrm{SM}} \\ \alpha\mathbf{d}_{\mathrm{GPS}} \\ 0 \end{pmatrix}. \tag{5}$$

The model parameter vector $\mathbf{m}$ is solved by the least-squares method. The hyperparameter α is the relative weight of GPS data against strong-motion data, and β is the strength of the smoothing constraint. Those hyperparameters are appropriately determined so as to minimize the Akaike's Bayesian information criterion (ABIC; Akaike, 1980) through a set of inversions by changing α and β. The ABIC for our problem is defined as

$$\begin{aligned} \mathrm{ABIC} = {} & (M_G + M_H + M_S - N) \log s(\tilde{\mathbf{m}}) \\ & - M_H \log \alpha^2 - M_S \log \beta^2 + \log \|\mathbf{G}^T\mathbf{G} \\ & + \alpha^2 \mathbf{H}^T\mathbf{H} + \beta^2 \mathbf{S}^T\mathbf{S}\| + C, \end{aligned} \tag{6}$$

$$s(\tilde{\mathbf{m}}) = \|\mathbf{d}_{\mathrm{SM}} - \mathbf{G}\tilde{\mathbf{m}}\|^2 + \alpha^2 \|\mathbf{d}_{\mathrm{GPS}} - \mathbf{H}\tilde{\mathbf{m}}\|^2 + \beta^2 \|\mathbf{S}\tilde{\mathbf{m}}\|^2, \tag{7}$$

where $\tilde{\mathbf{m}}$ is the estimated value of $\mathbf{m}$ (Asano *et al.*, 2005). C is a constant term independent of model parameter vector and hyperparameters.

Inversion Result

The distribution of the final-slip amount on the assumed fault surface estimated by the joint inversion is shown in Figure 6. The rupture starting point or hypocenter is indicated by the star in this figure. The rupture front propagation velocity, which triggers the rupture of the first time window, was selected to be 2.77 km/s, which is approximately 80% of the shear-wave velocity at the hypocenter. The hyperparameters α and β are, respectively, determined to be 90 and 0.06 by minimizing ABIC as shown in Figure 7.

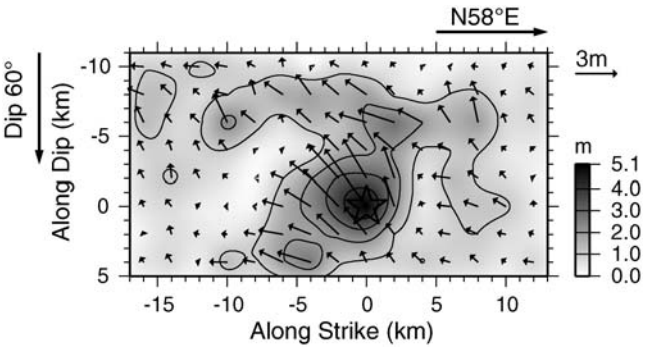

Figure 6. Final slip distribution on the fault plane with a contour interval of 1 m. The arrows show the slip vectors of the hanging wall relative to the footwall. The open star indicates the hypocenter or the rupture starting point.

The average amount of slip over the fault is 1.1 m. The total seismic moment was estimated to be 1.57×10^{19} N·m (M_{w} 6.7), which is consistent with the value by the moment-tensor solution of F-net (1.36×10^{19} N·m, M_{w} 6.7). The asperity or large slip area with the maximum slip of 5.1 m is observed at the subfault including the hypocenter, and it extends to the up-dip direction. The average slip of the asperity is about 2 m. The slip of the shallowest row is considerably small. The slip direction is almost oblique (~135°) around the hypocenter, while the right-lateral strike-slip component is relatively larger than the dip-slip component in the shallow portion of the fault plane.

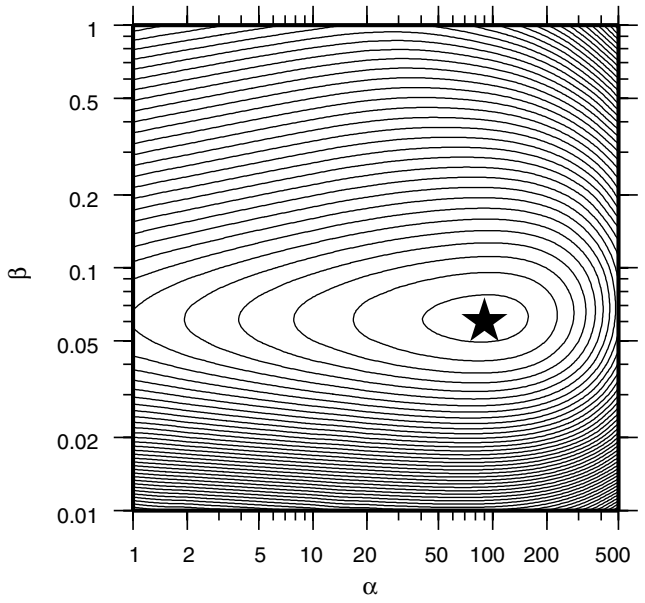

Figure 7. Contour map of ABIC as a function of α and β with a contour interval of 50. The point of ABIC minimum is indicated by the solid star.

The temporal progression of the slip at time steps of 1 s is shown in Figure 8. The rupture of the asperity lasted for approximately 4 s. The rupture mainly propagated to the up-dip direction and northeast in the shallow portion of the fault plane. The obtained moment-rate functions for each subfault are shown in Figure 9. The duration of the moment release of the subfaults in the asperity was approximately 2–2.5 s, and significant delay in the rupture propagation velocity was not observed. The total duration of the rupture is approximately 9 s.

Three components of the synthesized ground-velocity waveforms in 0.05–1.0 Hz are compared with the observed waveforms in Figure 10. The comparison between the observed and synthetic static horizontal displacement vectors at GPS stations is shown in Figure 11. The synthetic velocity waveforms and horizontal static displacements reproduce the observed ones well. The remarkable exception is that the amplitude of ISK002 and TYM002, where strong later phases are observed after the direct *S* wave, does not match the observed amplitude in the later phases. These amplitudes of the later phases are almost comparable to the amplitude of the *S* wave. It might be because our one-dimensional velocity-structure model could not always account for such complicated wave propagation at those stations.

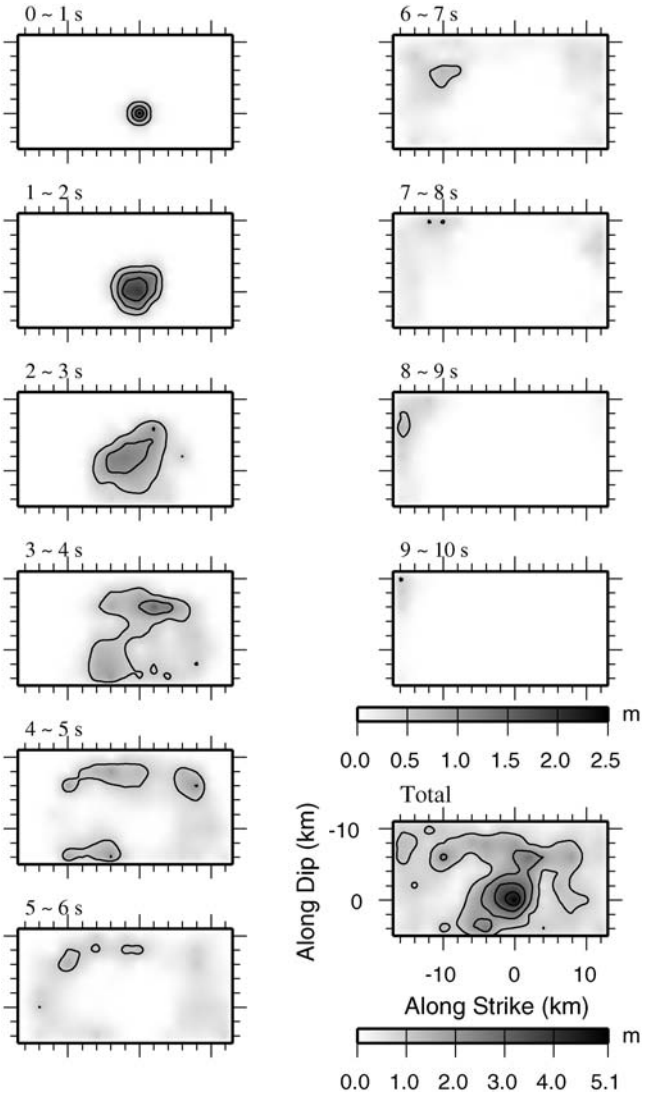

Figure 8. Snapshot of the temporal slip progression at time steps of 1 s. The open star indicates the rupture starting point.

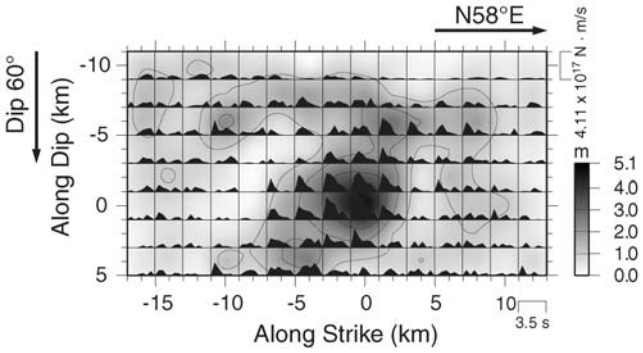

Figure 9. The obtained moment-rate functions of each subfault with the total slip distribution in the background. The open star indicates the rupture starting point.

In order to address the uncertainty of this source inversion, a set of resampling tests is performed, analyzing 1000 subsets generated by randomly removing three strong-motion stations and four GPS stations from the original dataset. Inverting 1000 subsets, 1000 solutions are independently obtained by the same kinematic source-inversion procedure described in the previous paragraphs. The optimum values of α and β range from 50 to 180 and 0.03 to 0.08, respectively, among 1000 cases. Figure 12 shows the average moment-rate functions of 1000 solutions and the standard deviation. The standard deviation of moment-rate functions at each subfault is not significant. The average of the total seismic moment is 1.64×10^{19} N·m, and the average of the maximum slip is 4.8 m; these are comparable to the best solution obtained from the whole dataset. Those coefficients of variation are 9% and 11%, respectively.

The concentration of the larger slip or asperity in and around the hypocenter as shown in Figure 6 is the same feature with the 2004 Mid-Niigata (Chuetsu) earthquake (Asano and Iwata, 2009), which occurred in the similar tectonic settings with the 2007 Noto Hanto earthquake. Both earthquakes ruptured the reverse faults, which have northeast–southwest strikes, and both earthquakes were regarded as the reactivation of the preexisting normal faults, which were formed during the back-arc rifting associated with the opening of the Japan Sea (Sato, 1994; Sato *et al.*, 2007). Such a concentrated asperity might cause relatively stronger *S* waves on the hanging-wall side according to the far-field *S*-wave radiation pattern from the reverse-slipping asperity. It is also consistent with the relatively high ratio of radiated energy to seismic moment for the 2004 Mid-Niigata and the 2007 Noto events estimated by Izutani (2005) and Izutani (2008).

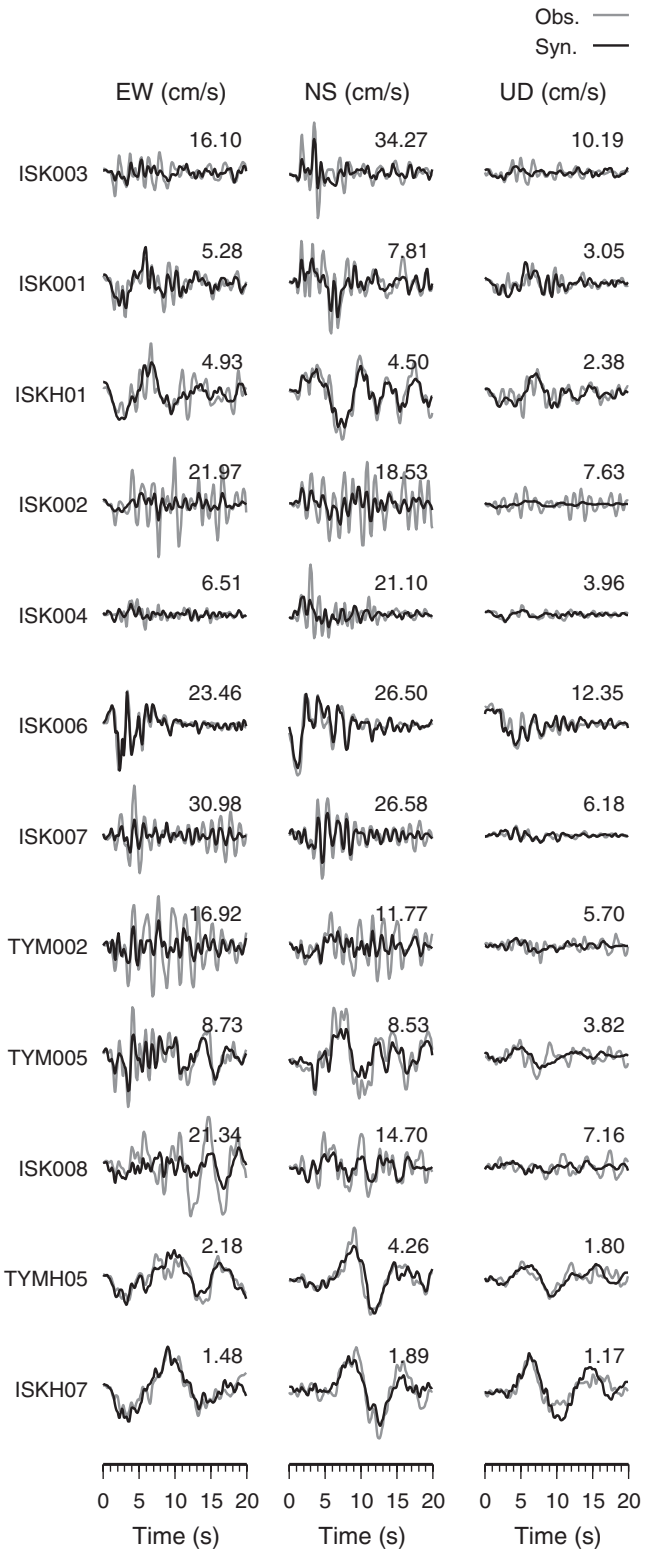

Figure 10. Comparison of strong-motion velocity waveforms in 0.05–1 Hz. Observed waveforms are plotted in gray, and synthetics generated from the source model obtained by the waveform inversion are plotted in black. The amplitude of waveforms is normalized by the maximum amplitude of the observation. The maximum amplitude of the observed waveforms is shown above each trace in cm/s. EW, east–west; NS, north–south; UD, up–down.

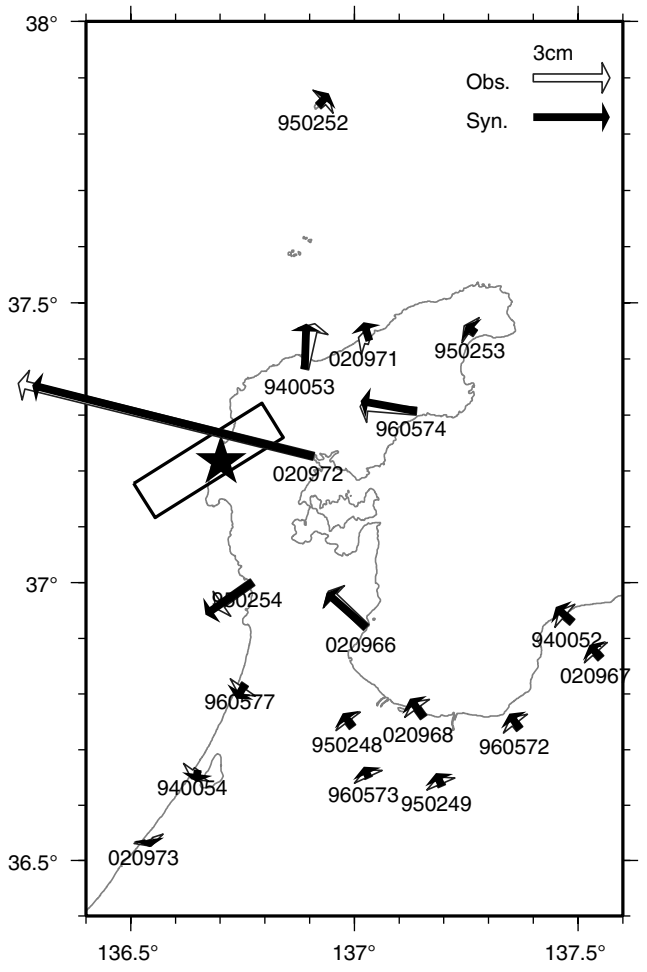

Figure 11. Comparison of static horizontal-displacement vectors at GPS stations between observation (open arrows) and synthetics (solid arrows). The solid star marks the epicenter of the 2007 Noto Hanto earthquake, and the rectangle indicates the surface projection of the source fault plane.

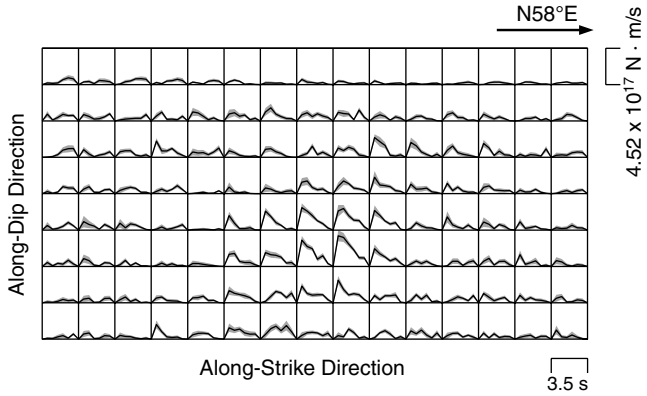

Figure 12. Average moment-rate functions of 1000 solutions (thick line) and those standard deviations (thin line) in the resampling test.

Discussion

Figure 13 compares the final slip distribution obtained by the joint inversion of the strong-motion static GPS data (Fig. 13a), obtained by the single dataset inversion of strong-motion data (Fig. 13b) and by the single dataset inversion of static GPS data (Fig. 13c). The overall feature of the slip distribution (i.e., the largest slip in the vicinity of hypocenter and the up-dip rupture propagation) are similar to each other. Note that the total number of GPS data is smaller than the total number of model parameters in this case or, the single inversion of GPS data shown in Fig. 13c is underdetermined and unstable if the same spatial model parameterization is used as the inversion of strong-motion data. In terms of data fitting for GPS data, the model from the joint inversion (Fig. 13a) fits better than the model from strong-motion data only (Fig. 13b) without much surprise.

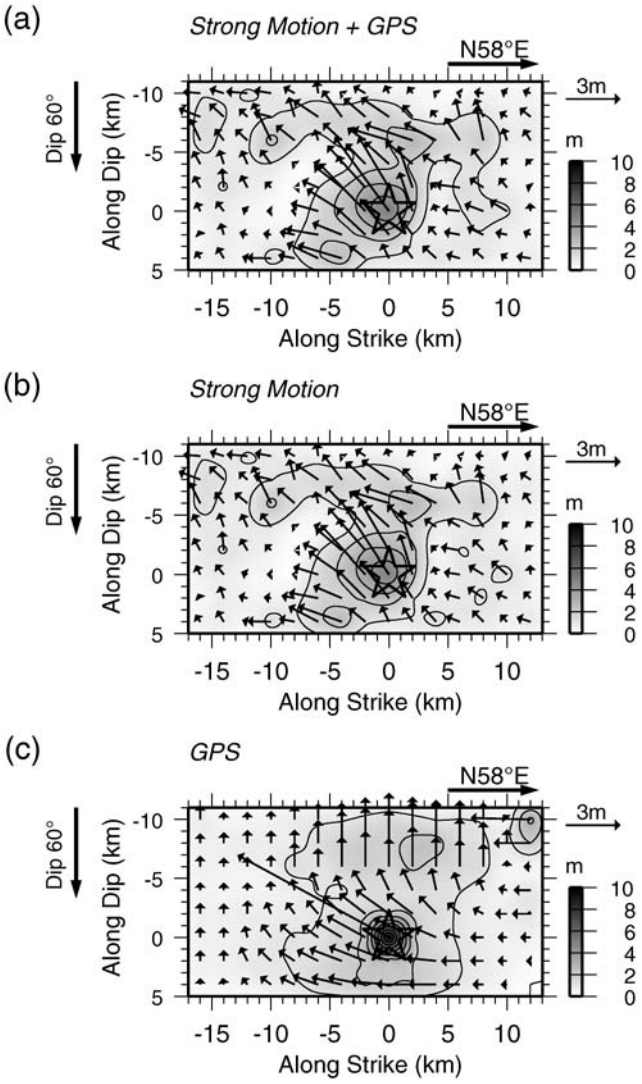

Figure 13. Comparison of the slip distributions obtained by (a) the joint inversion, (b) strong-motion data only, and (c) GPS data only.

The heterogeneous slip models of the 2007 Noto Hanto earthquake have been derived also in other studies by combined use of synthetic aperture interferometry (InSAR) and GPS data (Fukushima *et al.*, 2008; Ozawa *et al.*, 2008), strong-motion data (Aoi and Sekiguchi, 2007; Horikawa, 2008; Wu and Horiuchi, 2008), and combined use of strong-motion and GPS data (Momiyama *et al.*, 2009). The source models based on empirical Green's function methods are also proposed (Kurahashi *et al.*, 2008; Maeda *et al.*, 2008; Nozu, 2008; Shiba, 2008). Most of these studies found a large asperity in the vicinity of the hypocenter, which is consistent with our result. The slip distribution derived from InSAR and GPS data by Ozawa *et al.* (2008) is quite similar to that of our analysis in terms of the spatial slip distribution and slip vectors. The differences among source models may be attributed to many factors (e.g., inversion procedure, dataset, velocity-structure model, fault model settings, etc.). For the inversion using strong-motion data, the accuracy in the velocity-structure model for calculating Green's functions will greatly affect the result as seen in previous studies (e.g., Asano and Iwata, 2009). Because the velocity-structure model is carefully tuned up by waveform modeling, errors due to inaccuracy in the velocity-structure model are expected to be reduced in our source inversion.

As mentioned in the introductory section, some seafloor active faults have been recognized off the Noto peninsula by previous exploration studies using sonic prospecting and piston coring. According to Katagawa *et al.* (2005), the strike direction of these faults is northeast–southwest, and the length of F14, F15, and F16 faults are approximately 12 km, 11 km, and 11 km, respectively. In Figure 14, the locations of these seafloor active faults are plotted with the final slip distribution of the 2007 Noto Hanto earthquake. Strike angles of these seafloor active faults are consistent with that of the 2007 Noto Hanto earthquake. Based on their sonic prospecting, Katagawa *et al.* (2005) concluded that deformation due to the F14 fault reached the Holocene alluvium layer. Kato *et al.* (2008) obtained the seismic images, which illustrate that the contrast in velocity between the hanging wall and the footwall extends to a depth of approximately 10 km by the double-difference tomography method using densely observed aftershock data. They also pointed out that the surface extension of the mainshock fault plane imaged by the relocated aftershock distribution roughly corresponds to the surface traces of seafloor active faults (F14, F15, and F16). The large slip of the 2007 Noto Hanto earthquake obtained from the waveform inversion concentrates along the F14 fault and partially along the F15 fault as shown in Figure 14.

In Figure 14, the spatiotemporal aftershock distributions are also compared with the final slip distribution. The epicenters of aftershocks larger than M_{JMA} 2.0 determined by JMA in four periods are plotted on the map. The moment-tensor solutions determined by F-net of NIED for aftershocks larger than M_w 4.5 are also plotted in this figure. The locations of aftershock in the first hour correlate well with the large slip area of the mainshock along the F14 and F15 faults

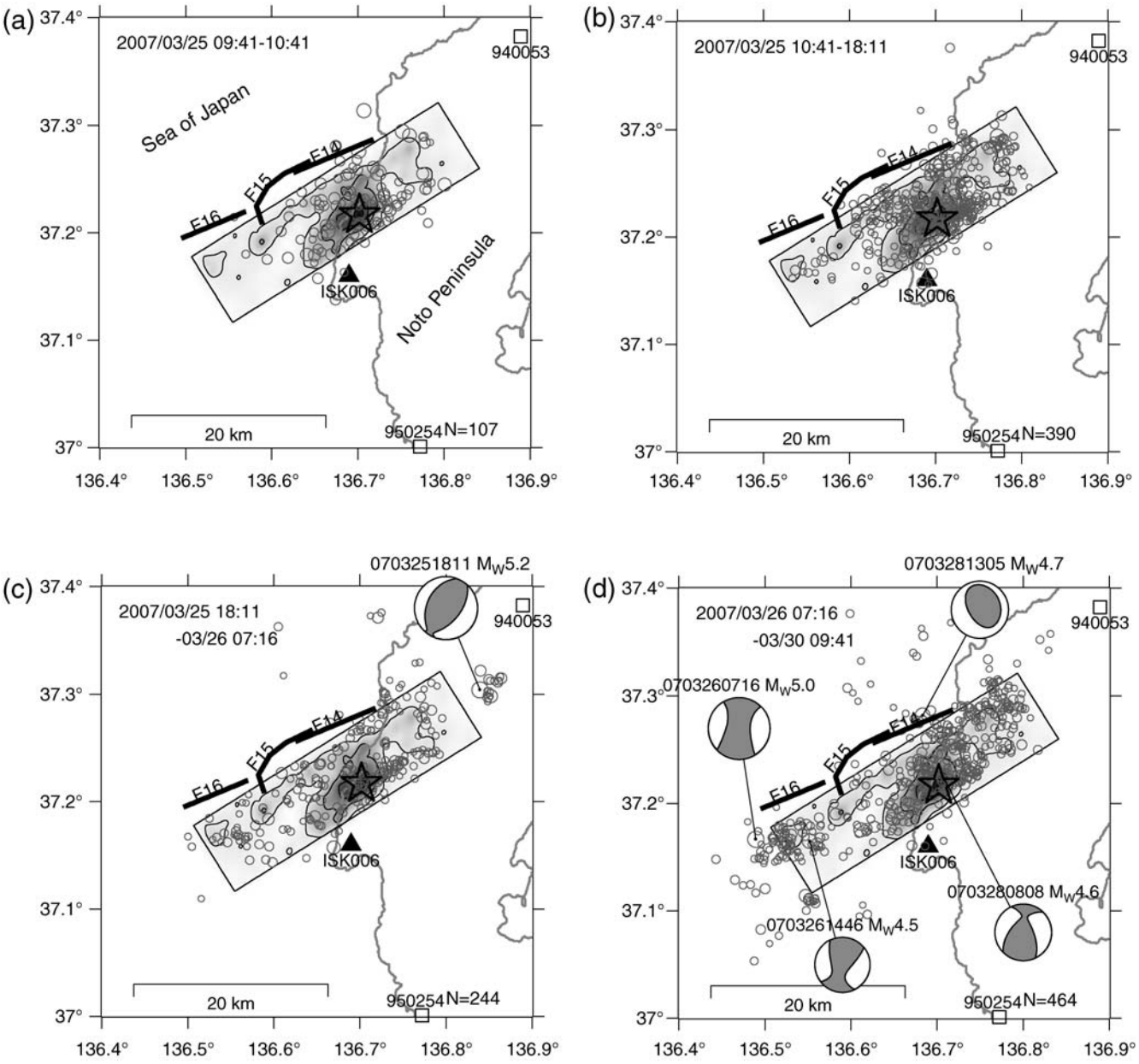

Figure 14. Map view of the final slip distribution compared with preexisting active fault traces and spatiotemporal distribution of the aftershock's epicenters greater than M_{JMA} 2.0 in each period. The open star indicates the epicenter of the mainshocks. The small open circles indicate the epicenters of aftershocks routinely located by JMA. The size of the circle is proportional to its magnitude (M_{JMA}). The thick lines labeled by F14, F15, and F16 are traces of seafloor active faults identified by Katagawa *et al.* (2005). The moment-tensor solutions determined by the F-net, NIED for aftershocks larger than M_w 4.5 are also shown in the map.

(Fig. 14a). This correlation demonstrates that the detailed slip distribution obtained in this study is precisely constrained by the combined use of strong-motion and GPS data and the well-calibrated Green's functions because the occurrence of early aftershocks are thought to be related to the fault rupture during the mainshock. Most aftershocks occurring within 8.5 hours are also located in and along the large slip area (Fig. 14b). The largest aftershock with M_w 5.2 occurred northeast off the rupture area of the mainshock at 18:11 on 25 March 2007 (Fig. 14c). No aftershock occurred adjacent to the largest aftershock before the occurrence of this largest aftershock. There is a gap of aftershock occurrence between the northeastern edge of the mainshock's rupture area and the aftershocks associated with the largest aftershock. Yoshimura *et al.* (2008) found a resistive block corresponding to this gap by the wideband magnetotelluric survey. This implies that the rupture of the mainshock blocked by such a material difference within the crust. After the occurrence of a large aftershock (M_w 5.0) at 07:16 on 26 March 2007 (JST) close to the southwestern edge of the F16 fault, the aftershock activity in that region also seems to be activated (Fig. 14d). The details of the spatial pattern of

aftershock distribution are also discussed in terms of static-stress change associated with the faulting by Toda (2008). Some of the large aftershocks occurring near the end of the extended rupture area obtained here seem to have non–double-couple components, and this might reflect the disturbance in the local stress field due to the coseismic effect of the rupture during the mainshock (Fig. 14).

From the results and comparison presented here, the 2007 Noto Hanto earthquake can be concluded as reactivation of preexisting F14 and F15 faults. The major rupture of the mainshock (asperity and its surrounding area) and the rupture areas of large aftershocks occupy a complementary area of causative source faults.

Conclusions

The source-rupture process of the 2007 Noto Hanto earthquake was estimated by the kinematic waveform inversion jointly using strong-motion data recorded at 12 near-source stations and GPS-measured static displacement data recorded at 19 GPS stations. The one-dimensional velocity-structure models for individual strong-motion stations are optimally modeled by waveform modeling of small aftershock records. The larger slips concentrate in the vicinity of the hypocenter and extend to the shallow portion of the source fault plane with a maximum slip of 5.1 m. The slip direction is almost oblique (~135°) around the hypocenter, while the right-lateral strike-slip component is dominant in the shallow portion of the assumed fault plane. The total seismic moment is 1.57×10^{19} N·m (M_w 6.7). The rupture of this event lasted approximately 9 s. The obtained source model explains observed strong ground motions and GPS-measured static horizontal displacements well. The slip distribution is well-correlated with the spatiotemporal aftershock distribution, and the northeast end of the rupture was blocked by the resistive structure in the crust. From these facts, the 2007 Noto Hanto earthquake can be concluded to be a reactivation of preexisting seafloor active faults, F14 and F15, which were revealed by the previous geophysical and geological surveys of Katagawa *et al.* (2005).

Data and Resources

Digital strong-motion data of K-NET and KiK-net can be obtained from NIED at www.kyoshin.bosai.go.jp (last accessed June 2010). The GPS-measured daily coordinate data of GEONET can be obtained from GSI at terras.gsi.go.jp (last accessed June 2010). The F-net moment tensor catalog was searched using www.fnet.bosai.go.jp/fnet/ (last accessed June 2010). Figures were drawn using the Generic Mapping Tools (Wessel and Smith, 1998).

Acknowledgments

The comments from Adrien Oth, an anonymous reviewer, and associate editor Arthur McGarr were quite helpful in improving the manuscript. This work is supported by a Grant-in-Aid for Scientific Research (B) Number 20310105 (PI T. Iwata) and a Grant-in-Aid for Young Scientists (Start-Up) Number 19810008 and (B) Number 22710172 (PI K. Asano) from the Japan Society for the Promotion of Science.

References

Akaike, H. (1980). Likelihood and the Bayes procedure, in *Bayesian Statistics*, J. M. Bernardo, M. H. DeGroot, D. V. Lindley, and A. F. M. Smith (Editors), University Press, Valencia, Spain, 143–166.

Aoi, S., and H. Sekiguchi (2007). Source process of the 2007 Noto-Hanto earthquake derived from near-fault strong motion data, *Rep. Coord. Comm. Earthq. Pred.* **78,** 378–381 (in Japanese).

Aoi, S., K. Obara, S. Hori, K. Kasahara, and Y. Okada (2000). New Japanese uphole/downhole strong-motion observation network: KiK-net, *Seismol. Res. Lett.* **72,** 239.

Aoki, H., T. Tada, Y. Sasaki, T. Ooida, I. Muramatsu, H. Shimamura, and I. Furuya (1972). Crustal structure in the profile across central Japan as derived from explosion seismic observations, *J. Phys. Earth* **20,** 197–223.

Asano, K., and T. Iwata (2009). Source rupture process of the 2004 Chuetsu, mid Niigata prefecture, Japan, earthquake inferred from waveform inversion with dense strong motion data, *Bull. Seismol. Soc. Am.* **99,** 123–140.

Asano, K., T. Iwata, and K. Irikura (2005). Estimation of source rupture process and strong ground motion simulation of the 2002 Denali, Alaska, earthquake, *Bull. Seismol. Soc. Am.* **95,** 1701–1715.

Bouchon, M. (1981). A simple method to calculate Green's functions for elastic layered media, *Bull. Seismol. Soc. Am.* **71,** 959–971.

Carroll, D. L. (1996). Genetic algorithms and optimizing chemical oxygen-iodine lasers, in *Developments in Theoretical and Applied Mechanics*, H. B. Wilson, R. C. Batra, C. W. Bert, A. M. J. Davis, R. A. Schapery, D. S. Stewart, and F. F. Swinson (Editors), School of Engineering, University of Alabama, Tuscaloosa, Alabama, Vol. 18, 411–424.

Fukushima, Y., T. Ozawa, and M. Hashimoto (2008). Fault model of the 2007 Noto Hanto earthquake estimated from PALSAR radar interferometry and GPS data, *Earth Planets Space* **60,** 99–104.

Fukuyama, E., M. Ishida, D. S. Dreger, and H. Kawai (1998). Automated seismic moment tensor determination by using on-line broadband seismic waveforms, *Zisin (J. Seism. Soc. Jpn.)* **51,** 149–156 (in Japanese with English abstract).

Hartzell, S. H., and T. H. Heaton (1983). Inversion of strong ground motion and teleseismic waveform data for the fault rupture history of the 1979 Imperial Valley, Carifornia, earthquake, *Bull. Seismol. Soc. Am.* **73,** 1553–1583.

Holland, J. H. (1975). *Adaptation in Natural and Artificial Systems*, University of Michigan Press, Ann Arbor, 183 pp.

Horikawa, H. (2008). Characterization of the 2007 Noto Hanto, Japan, earthquake, *Earth Planets Space* **60,** 1017–1022.

Ishimoto, M., and T. Yutsudo (2007). Crustal deformation of the Noto Hanto earthquake in 2007 observed by GEONET, *J. Geograph. Surv. Inst.* **113,** 37–39 (in Japanese).

Iwata, T., K. Asano, M. Kuriyama, and A. Iwaki (2008). Non-linear site response characteristics of K-NET ISK005 station and relation to earthquake disaster during the 2007 Noto Hanto earthquake, central Japan, *Proc. Fourteenth World Conf. Earthq. Eng.*, paper No. 01-1026 (DVD-ROM).

Izutani, Y. (2005). Radiated energy from the mid Niigata, Japan, earthquake of October 23, 2004, and its aftershocks, *Geophys. Res. Lett.* **32,** L21313, doi 10.1029/2005GL024116.

Izutani, Y. (2008). Radiated energy from the Noto Hanto, Japan, earthquake of March 25, 2007, and its aftershock, *Earth Planets Space* **60,** 145–150.

Kanno, T., S. Senna, N. Morikawa, A. Narita, and H. Fujiwara (2003). 3-D underground structure model in Kanazawa region, *BUTSURI-TANSA (Geophys. Explor.)* **56,** 313–326 (in Japanese with English abstract).

Katagawa, H., M. Hamada, S. Yoshida, H. Kadosawa, A. Mitsuhashi, Y. Kono, and Y. Kinugasa (2005). Geological development of the west

sea area of the Noto peninsula district in the Neogene Tertiary to Quaternary, central Japan, *J. Geogr.* **114,** 791–810 (in Japanese with English abstract).

Kato, A., S. Sakai, T. Iidaka, T. Iwasaki, E. Kurashimo, T. Igarashi, N. Hirata, T. Kanazawa, and The group for the joint aftershock observation of the 2007 Noto Hanto Earthquake (2008). Three-dimensional velocity structure in the source region of the Noto Hanto Earthquake in 2007 imaged by a dense seismic observation, *Earth Planets Space* **60,** 105–110.

Kennett, B. L. N., and N. J. Kerry (1979). Seismic waves in a stratified half space, *Geophys. J. R. Astr. Soc.* **57,** 557–583.

Kinoshita, S. (1998). Kyoshin-net (K-NET), *Seismol. Res. Lett.* **69,** 309–332.

Kurahashi, S., K. Masaki, and K. Irikura (2008). Source model of the 2007 Noto-Hanto earthquake (M_w 6.7) for estimating broad-band strong ground motion, *Earth Planets Space* **60,** 89–94.

Lawson, C. L., and R. J. Hanson (1974). *Solving Least Squares Problems*, Prentice-Hall, New Jersey, 340 pp.

Maeda, T., M. Ichiyanagi, H. Takahashi, R. Honda, T. Yamaguchi, M. Kasahara, and T. Sasatani (2008). Source parameters of the 2007 Noto Hanto earthquake sequence derived from strong motion records at temporary and permanent stations, *Earth Planets Space* **60,** 1011–1016.

Momiyama, S., K. Hikima, and K. Koketsu (2009). Joint inversion for the source process of the 2007 Noto Hanto earthquake with improved velocity structure models, *Abstr. Jpn. Geosci. Union Meet. 2009*, S148-P006 (CD-ROM).

Nishida, S., C. Scawthorn, J. Kiyono, and T. Tsutsumiuchi (2007). Noto Peninsula (Japan) earthquake of March 25, 2007, *EERI Spec. Earthq. Rept.*, 4 pp.

Nozu, A. (2008). Rupture process of the 2007 Noto Hanto earthquake: waveform inversion using empirical Green's function, *Earth Planets Space* **60,** 1029–1034.

Okamura, Y. (2007). Geological Map West of Noto Peninsula, *Marine Geol. Map Ser.* **61,** Geological Survey of Japan, AIST (CD-ROM).

Ozawa, S., H. Yarai, M. Tobita, H. Une, and T. Nishimura (2008). Crustal deformation associated with the Noto Hanto Earthquake in 2007 in Japan, *Earth Planets Space* **60,** 95–98.

Sakai, S., A. Kato, T. Iidaka, T. Iwasaki, E. Kurashimo, T. Igarashi, N. Hirata, T. Kanazawa, and The group for the joint aftershock observation of the 2007 Noto Hanto Earthquake (2008). Highly resolved distribution of aftershocks of the 2007 Noto Hanto Earthquake by a dense seismic observation, *Earth Planets Space* **60,** 83–88.

Sato, H. (1994). The relationship between late Cenozoic tectonic events and stress field and basin development in northeastern Japan, *J. Geophys. Res.* **99,** 22,261–22,274.

Sato, H., T. Iwasaki, T. Kanazawa, S. Miyazaki, N. Kato, S. Sakai, T. Yamada, T. Miyauchi, T. Ito, and N. Hirata (2007). Characterization of the 2007 Noto Hanto earthquake, central Japan: Insights from seismic profiling, aftershock observations, and co-seismic crustal deformation, *Bull. Earthq. Res. Inst., Univ. Tokyo* **82,** 369–379.

Sekiguchi, H., K. Irikura, and T. Iwata (2000). Fault geometry in the rupture termination of the 1995 Hyogo-ken Nanbu earthquake, *Bull. Seismol. Soc. Am.* **90,** 117–133.

Sen, M. K., and P. L. Stoffa (1991). Nonlinear one-dimensional seismic waveform inversion using simulated annealing, *Geophysics* **56,** 1624–1638.

Shiba, Y. (2008). Rupture process during the 2007 Noto Hanto earthquake (M_{JMA} 6.9) and strong-motion simulation in the source region, *Earth Planets Space* **60,** 1023–1028.

Toda, S. (2008). Coulomb stresses imparted by the 25 March 2007 $M_w = 6.6$ Noto-Hanto, Japan, earthquake explain its 'butterfly' distribution of aftershocks and suggest a heightened seismic hazard, *Earth Planets Space* **60,** 1041–1046.

Wald, D. J., and R. W. Graves (2001). Resolution analysis of finite fault source inversion using one- and three-dimensional Green's functions, 2. Combining seismic and geodetic data, *J. Geophys. Res.* **106,** 8767–8788.

Wessel, P., and W. H. F. Smith (1998). New, improved version of Generic Mapping Tools released, *Eos Trans. AGU* **79,** 579.

Wu, C., and S. Horiuchi (2008). Automatic determination of source parameters of the 2007 Noto Hanto earthquake, *Earth Planets Space* **60,** 1053–1057.

Yamada, M., S.-C. Park, and J. Mori (2008). The 2007 Noto peninsula, Japan, earthquake (M_w 6.7): Damage to wooden structures, *Seismol. Res. Lett.* **79,** 20–24.

Yoshimura, R., N. Oshiman, M. Uyeshima, Y. Ogawa, M, Mishina, H. Toh, S. Sakanaka, H. Ichihara, I. Shiozaki, T. Ogawa, T. Miura, S. Koyama, Y. Fujita, K. Nishimura, Y. Takagi, M. Imai, R. Honda, S. Yabe, S. Nagaoka, M. Tada, and T. Mogi (2008). Magnetotelluric observations around the focal region of the 2007 Noto Hanto earthquake (M_j 6.9), central Japan, *Earth Planets Space* **60,** 117–122.

Disaster Prevention Research Institute
Kyoto University
Gokasho, Uji
Kyoto 611-0011, Japan
k-asano@egmdpri01.dpri.kyoto-u.ac.jp
iwata@egmdpri01.dpri.kyoto-u.ac.jp

Manuscript received 17 September 2010